

1 **LEAST-SQUARES NEURAL NETWORK (LSNN) METHOD**
2 **FOR SCALAR NONLINEAR HYPERBOLIC CONSERVATION LAWS:**
3 **DISCRETE DIVERGENCE OPERATOR***

4 ZHIQIANG CAI[†], JINGSHUANG CHEN[†], AND MIN LIU[‡]

5 **Abstract.** A least-squares neural network (LSNN) method was introduced for solving scalar linear and nonlinear
6 hyperbolic conservation laws (HCLs) in [7, 6]. This method is based on an equivalent least-squares (LS) formulation
7 and uses ReLU neural network as approximating functions, making it ideal for approximating discontinuous functions
8 with unknown interface location. In the design of the LSNN method for HCLs, the numerical approximation of
9 differential operators is a critical factor, and standard numerical or automatic differentiation along coordinate
10 directions can often lead to a failed NN-based method. To overcome this challenge, this paper rewrites HCLs in
11 their divergence form of space and time and introduces a new discrete divergence operator. As a result, the proposed
12 LSNN method is free of penalization of artificial viscosity.

13 Theoretically, the accuracy of the discrete divergence operator is estimated even for discontinuous solutions.
14 Numerically, the LSNN method with the new discrete divergence operator was tested for several benchmark problems
15 with both convex and non-convex fluxes, and was able to compute the correct physical solution for problems with
16 rarefaction, shock or compound waves. The method is capable of capturing the shock of the underlying problem
17 without oscillation or smearing, even without any penalization of the entropy condition, total variation, and/or
18 artificial viscosity.

19 **Key words.** discrete divergence operator, least-squares method, ReLU neural network, scalar nonlinear hy-
20 perbolic conservation law

21 **AMS subject classifications.**

22 **1. Introduction.** Numerically approximating solutions of nonlinear hyperbolic conservation
23 laws (HCLs) is a computationally challenging task. This is partly due to the discontinuous nature
24 of HCL solutions at unknown locations, which makes approximation using fixed, quasi-uniform
25 meshes very difficult. Over the past five decades, many advanced numerical methods have been
26 developed to address this issue, including higher order finite volume/difference methods using
27 limiters, filters, ENO/WENO, etc.(e.g., [31, 33, 32, 16, 19, 20, 25]) and discontinuous and/or
28 adaptive finite element methods (e.g., [10, 3, 11, 14, 4, 21, 22]).

29 Neural networks (NNs) as a new class of approximating functions have been used recently for
30 solving partial differential equations (see, e.g., [9, 30, 34]) due to their versatile expressive power.
31 One of the unique features of NNs is their ability to generate moving meshes implicitly by neurons
32 that can automatically adapt to the target function and the solution of a PDE, which helps over-
33 come the limitations of traditional approximation methods that use fixed meshes. For example, a
34 ReLU NN generates continuous piece-wise linear functions with irregular and free/moving meshes.
35 This property of ReLU NNs was used in [7] for solving linear advection-reaction problem with dis-
36 continuous solution, without requiring information about the location of discontinuous interfaces.
37 Specifically, the least-squares NN method studied in [7] is based on the least-squares formulation in
38 ([2, 12]), and it uses ReLU NNs as the approximating functions while approximating the differential
39 operator by directional numerical differentiation. Compared to various adaptive mesh refinement
40 (AMR) methods that locate discontinuous interfaces through an adaptive mesh refinement process,
41 the LSNN method is significant more efficient in terms of the number of degrees of freedom (DoF)
42 used.

43 Solutions to nonlinear hyperbolic conservation laws are often discontinuous due to shock for-

*This work was supported in part by the National Science Foundation under grant DMS-2110571.

[†]Department of Mathematics, Purdue University, 150 N. University Street, West Lafayette, IN 47907-2067
(caiz@purdue.edu, chen2042@purdue.edu).

[‡]School of Mechanical Engineering, Purdue University, 585 Purdue Mall, West Lafayette, IN 47907-
2088(liu66@purdue.edu).

44 mation. It is well-known that the differential form of a HCL is not valid at shock waves, where the
 45 solution is discontinuous. As a result, the directional numerical differentiation of the differential
 46 operator based on the differential form used in [7] cannot be applied to nonlinear HCLs. To over-
 47 come this challenge, the integral form of HCLs (as seen in [25]) must be used, which is valid for
 48 problems with discontinuous solutions, particularly at the discontinuous interfaces. This is why
 49 the integral form forms the basis of many conservative methods such as Roe’s scheme [18], WENO
 50 [32, 33], etc.

51 Approximating the divergence operator by making use of the Roe and ENO fluxes, in [6] we
 52 tested the resulting LSNN method for scalar nonlinear HCLs. Numerical results for the inviscid
 53 Burgers equation showed that the LSNN method with conservative numerical differentiation is
 54 capable of capturing the shock without smearing and oscillation. Additionally, the LSNN method
 55 has fewer DoF than traditional mesh-based methods. Despite the promising results in [6], limita-
 56 tions were observed with the LSNN method when using conservative numerical differentiation of
 57 the Roe and second-order ENO fluxes. For example, the resulting LSNN method is not accurate
 58 for complicated initial condition, and has problems with rarefaction waves and non-convex spatial
 59 fluxes. To improve accuracy, using “higher order” conservative methods such as ENO or WENO
 60 could be considered. However, these conservative schemes are designed for traditional mesh-based
 61 methods and the “higher order” here is measured at where solutions are smooth.

62 In this paper, a new discrete divergence operator is proposed to accurately approximate the
 63 divergence of a vector field even in the presence of discontinuities. This operator is defined based on
 64 its physical meaning: the rate of net outward flux per unit volume, and is approximated through
 65 surface integrals by the *composite* mid-point/trapezoidal numerical integration. Theoretically,
 66 the accuracy of the discrete divergence operator can be improved by increasing the number of
 67 surface integration points (as shown in Lemma 4.3 and Remark 4.4). The LSNN method, being a
 68 “mesh/point-free” space-time method, allows the use of all points on the boundary surfaces of a
 69 control volume for numerical integration.

70 Theoretically, we show that the residual of the LSNN approximation using the newly developed
 71 discrete divergence operator is bounded by the best approximation of the class of NN functions
 72 in some measure as stated in Lemma 3.1 plus the approximation error from numerical integration
 73 and differentiation (Lemma 3.3). Numerically, our results show that the LSNN method with the
 74 new discrete divergence operator can accurately solve the inviscid Burgers equation with various
 75 initial conditions, compute the viscosity vanishing solution, capture shock without oscillation or
 76 smearing, and is much more accurate than the LSNN method in [6]. Note that the LSNN method
 77 does not use flux limiters. Moreover, the LSNN method using new discrete divergence operator
 78 works well for problems with non-convex flux and accurately simulates compound waves.

79 Recently, several NN-based numerical methods have been introduced for solving scalar nonlin-
 80 ear hyperbolic conservation laws by various researchers ([1, 5, 6, 7, 15, 30, 29]). Those methods can
 81 be categorized as the physics informed neural network (PINN) [1, 15, 30, 29] and the least-squares
 82 neural network (LSNN) [5, 6, 7, 9] methods. First, both methods are based on the least-squares
 83 principle, but the PINN uses the discrete l^2 norm and the LSNN uses the continuous Sobolev norm
 84 depending on the underlying problem. Second, the differential operator of the underlying prob-
 85 lem is approximated by either automatic differentiation or standard finite difference quotient for
 86 the PINN and by specially designed discrete differential operator for the LSNN. For example, the
 87 LSNN uses discrete directional differential operator in [7] for linear advection-reaction problems,
 88 and various traditional conservative schemes in [6] or discrete divergence operator in this paper
 89 (see [5] for its first version) for nonlinear scalar hyperbolic conservation laws.

90 The original PINN has limitations that have been addressed in several studies (see, e.g., [15,
 91 29]). For nonlinear scalar hyperbolic conservation laws, [15] found that the PINN fails to provide
 92 reasonable approximate solution of the PDE and modified the loss function by penalizing the
 93 artificial viscosity term. [29] applied the discrete l^2 norm to the boundary integral equations over

94 control volumes instead of the differential equations over points and modified the loss function by
 95 penalizing the entropy, total variation, and/or artificial viscosity. Even though the least-squares
 96 principle permits freedom of various penalizations, choosing proper penalization constants can
 97 be challenging in practice and it affects the accuracy, efficiency, and stability of the method. In
 98 contrast, the LSNN does not require any penalization constants.

99 The paper is organized as follows. Section 2 describes the hyperbolic conservation law, its
 100 least-squares formulation, and preliminaries. The space-time LSNN method and its block version
 101 are presented in Sections 3. The discrete divergence operator and its error bound is introduced and
 102 analyzed in Section 4. Finally, numerical results for various benchmark test problems are given in
 103 Section 5.

104 **2. Problem Formulation.** Let $\tilde{\Omega}$ be a bounded domain in \mathbb{R}^d ($d = 1, 2, \text{ or } 3$) with Lipschitz
 105 boundary, and $I = (0, T)$ be the temporal interval. Consider the scalar nonlinear hyperbolic
 106 conservation law

$$107 \quad (2.1) \quad \begin{cases} u_t(\mathbf{x}, t) + \nabla_{\mathbf{x}} \cdot \tilde{\mathbf{f}}(u) = 0, & \text{in } \tilde{\Omega} \times I, \\ u = \tilde{g}, & \text{on } \tilde{\Gamma}_-, \\ u(\mathbf{x}, 0) = u_0(\mathbf{x}), & \text{in } \tilde{\Omega}, \end{cases}$$

108 where u_t is the partial derivative of u with respect to the temporal variable t ; $\nabla_{\mathbf{x}} \cdot$ is a divergence
 109 operator with respect to the spatial variable \mathbf{x} ; $\tilde{\mathbf{f}}(u) = (f_1(u), \dots, f_d(u))$ is the spatial flux vector
 110 field; $\tilde{\Gamma}_-$ is the part of the boundary $\partial\tilde{\Omega} \times I$ where the characteristic curves enter the domain $\tilde{\Omega} \times I$;
 111 and the boundary data \tilde{g} and the initial data u_0 are given scalar-valued functions. Without loss
 112 of generality, assume that $f_i(u)$ is twice differentiable for $i = 1, \dots, d$.

113 Problem (2.1) is a hyperbolic partial differential equation defined on a space-time domain
 114 $\Omega = \tilde{\Omega} \times I$ in \mathbb{R}^{d+1} . Denote the inflow boundary of the domain Ω and the inflow boundary
 115 condition by

$$116 \quad \Gamma_- = \begin{cases} \tilde{\Gamma}_-, & t \in (0, T), \\ \Omega, & t = 0 \end{cases} \quad \text{and} \quad g = \begin{cases} \tilde{g}, & \text{on } \tilde{\Gamma}_-, \\ u_0(\mathbf{x}), & \text{on } \Omega, \end{cases}$$

117 respectively. Then (2.1) may be rewritten as the following compact form

$$118 \quad (2.2) \quad \begin{cases} \mathbf{div} \mathbf{f}(u) = 0, & \text{in } \Omega \in \mathbb{R}^{d+1}, \\ u = g, & \text{on } \Gamma_-, \end{cases}$$

119 where $\mathbf{div} = (\partial_{x_1}, \dots, \partial_{x_d}, \partial_t)$ is a divergence operator with respect to both spatial and temporal
 120 variables $\mathbf{z} = (\mathbf{x}, t)$, and $\mathbf{f}(u) = (f_1(u), \dots, f_d(u), u) = (\tilde{\mathbf{f}}(u), u)$ is the spatial and temporal flux
 121 vector field. Assume that $u \in L^\infty(\Omega)$. Then u is called a weak solution of (2.2) if and only if

$$122 \quad (2.3) \quad -(\mathbf{f}(u), \nabla \varphi)_{0, \Omega} + (\mathbf{n} \cdot \mathbf{f}(u), \varphi)_{0, \Gamma_-} = 0, \quad \forall \varphi \in C_{\Gamma_+}^1(\bar{\omega}),$$

123 where $\Gamma_+ = \partial\Omega \setminus \Gamma_-$ is the outflow boundary and $C_{\Gamma_+}^1(\bar{\omega}) = \{\varphi \in C^1(\bar{\omega}) : \varphi = 0 \text{ on } \Gamma_+\}$.

124 Denote the collection of square integrable vector fields whose divergence is also square inte-
 125 grable by

$$126 \quad H(\mathbf{div}; \Omega) = \{\boldsymbol{\tau} \in L^2(\Omega)^{d+1} \mid \mathbf{div} \boldsymbol{\tau} \in L^2(\Omega)\}.$$

127 It is then easy to see that solutions of (2.2) are in the following subset of $L^2(\Omega)$

$$128 \quad (2.4) \quad \mathcal{V}_{\mathbf{f}} = \{v \in L^2(\Omega) \mid \mathbf{f}(v) \in H(\mathbf{div}; \Omega)\}.$$

129 Define the least-squares (LS) functional

$$130 \quad (2.5) \quad \mathcal{L}(v; g) = \|\mathbf{div} \mathbf{f}(v)\|_{0, \Omega}^2 + \|v - g\|_{0, \Gamma_-}^2,$$

131 where $\|\cdot\|_{0,S}$ denotes the standard $L^2(S)$ norm for $S = \Omega$ and Γ_- . Now, the corresponding
 132 least-squares formulation is to seek $u \in V_{\mathbf{f}}$ such that

$$133 \quad (2.6) \quad \mathcal{L}(u; g) = \min_{v \in V_{\mathbf{f}}} \mathcal{L}(v; g).$$

134 **PROPOSITION 2.1.** *Assume that $u \in L^\infty(\Omega)$ is a piece-wise C^1 function. Then u is a weak
 135 solution of (2.2) if and only if u is a solution of the minimization problem in (2.6).*

136 *Proof.* The proposition is a direct consequence of Theorem 2.5 in [13]. \square

137 **3. Least-Squares Neural Network Method.** Based on the least-squares formulation in
 138 (2.6), in this section we first describe the least-squares neural network (LSNN) method for the scalar
 139 nonlinear hyperbolic conservation law and then estimate upper bound of the LSNN approximation.

140 To this end, denote a scalar-valued function generated by a l -layer fully connected neural
 141 network by

$$142 \quad (3.1) \quad \mathcal{N}(\mathbf{z}) = \boldsymbol{\omega}^{(l)} \left(N^{(l-1)} \circ \dots \circ N^{(2)} \circ N^{(1)}(\mathbf{z}) \right) - b^{(l)} : \mathbf{z} = (\mathbf{x}, t) \in \mathbb{R}^{d+1} \longrightarrow \mathbb{R},$$

143 where $\boldsymbol{\omega}^{(l)} \in \mathbb{R}^{n_{l-1}}$, $b^{(l)} \in \mathbb{R}$, and the symbol \circ denotes the composition of functions. For $k =$
 144 $1, \dots, l-1$, the $N^{(k)} : \mathbb{R}^{n_{k-1}} \rightarrow \mathbb{R}^{n_k}$ is called the k^{th} hidden layer of the network defined as
 145 follows:

$$146 \quad (3.2) \quad N^{(k)}(\mathbf{z}^{(k-1)}) = \tau(\boldsymbol{\omega}^{(k)} \mathbf{z}^{(k-1)} - \mathbf{b}^{(k)}) \quad \text{for } \mathbf{z}^{(k-1)} \in \mathbb{R}^{n_{k-1}},$$

147 where $\boldsymbol{\omega}^{(k)} \in \mathbb{R}^{n_k \times n_{k-1}}$, $\mathbf{b}^{(k)} \in \mathbb{R}^{n_k}$, $\mathbf{z}^{(0)} = \mathbf{z}$, and $\tau(s)$ is the activation function whose application
 148 to a vector is defined component-wisely. In this paper, we will use the rectified linear unit (ReLU)
 149 activation function given by

$$150 \quad (3.3) \quad \tau(s) = \max\{0, s\} = \begin{cases} 0, & \text{if } s \leq 0, \\ s, & \text{if } s > 0. \end{cases}$$

151 As shown in [7], the ReLU is a desired activation function for approximating discontinuous solution.

152 Denote the set of neural network functions by

$$153 \quad \mathcal{M}_N = \mathcal{M}_N(l) = \{ \mathcal{N}(\mathbf{z}) \text{ defined in (3.1)} : \boldsymbol{\omega}^{(k)} \in \mathbb{R}^{n_k \times n_{k-1}}, \mathbf{b}^{(k)} \in \mathbb{R}^{n_k} \text{ for } k = 1, \dots, l \},$$

154 where the subscript N denotes the total number of parameters $\boldsymbol{\theta} = \{ \boldsymbol{\omega}^{(k)}, \mathbf{b}^{(k)} \}$ given by

$$155 \quad N = M_d(l) = \sum_{k=1}^l n_k \times (n_{k-1} + 1).$$

156 Obviously, the continuity of the activation function $\tau(s)$ implies that \mathcal{M}_N is a subset of $C^0(\Omega)$.
 157 Together with the smoothness assumption on spatial flux $\tilde{\mathbf{f}}(u)$, it is easy to see that \mathcal{M}_N is also a
 158 subset of $\mathcal{V}_{\mathbf{f}}$ defined in (2.4).

159 Since \mathcal{M}_N is not a linear subspace, it is then natural to discretize the HCL using a least-
 160 squares minimization formulation. Before defining the computationally feasible least-squares neu-
 161 ral network (LSNN) method, let us first consider an intermediate least-squares neural network
 162 approximation: finding $u^N(\mathbf{z}; \boldsymbol{\theta}^*) \in \mathcal{M}_N$ such that

$$163 \quad (3.4) \quad \mathcal{L}(u^N(\cdot; \boldsymbol{\theta}^*); g) = \min_{v \in \mathcal{M}_N} \mathcal{L}(v(\cdot; \boldsymbol{\theta}); g) = \min_{\boldsymbol{\theta} \in \mathbb{R}^N} \mathcal{L}(v(\cdot; \boldsymbol{\theta}); g).$$

164 LEMMA 3.1. Let u be the solution of (2.2), and let $u^N \in \mathcal{M}_N$ be a solution of (3.4). Assume
 165 that \mathbf{f} is twice differentiable, then there exists a positive constant C such that

$$\begin{aligned} \mathcal{L}(u^N; g) &= \inf_{v \in \mathcal{M}_N} \left(\|v - u\|_{0, \Gamma_-}^2 + \|\mathbf{div} [\mathbf{f}(v) - \mathbf{f}(u)]\|_{0, \Omega}^2 \right) \\ (3.5) \quad &\leq C \inf_{v \in \mathcal{M}_N} \left(\|v - u\|_{0, \Gamma_-}^2 + \|\mathbf{div} [\mathbf{f}'(u)(v - u)]\|_{0, \Omega}^2 \right) + h.o.t., \end{aligned}$$

167 where *h.o.t.* means a higher order term comparing to the first term.

168 *Proof.* For any $v \in \mathcal{M}_N$, (3.4) and (2.2) imply that

$$169 \quad \mathcal{L}(u^N; g) \leq \mathcal{L}(v; g) = \|v - u\|_{0, \Gamma_-}^2 + \|\mathbf{div} [\mathbf{f}(v) - \mathbf{f}(u)]\|_{0, \Omega}^2,$$

170 which proves the validity of the equality in (3.5). By the Taylor expansion, there exists $\{w_i\}_{i=1}^d$
 171 between u and v such that

$$172 \quad \mathbf{f}(v) - \mathbf{f}(u) = \mathbf{f}'(u)(v - u) + \frac{1}{2} \mathbf{f}''(w)(v - u)^2,$$

173 where $\mathbf{f}'(u) = (f'_1(u), \dots, f'_d(u), 1)^t$ and $\mathbf{f}''(w) = (f''_1(w_1), \dots, f''_d(w_d), 0)^t$. Together with the
 174 triangle inequality we have

$$175 \quad (3.6) \quad \|\mathbf{div} [\mathbf{f}(v) - \mathbf{f}(u)]\|_{0, \Omega} \leq \|\mathbf{div} [\mathbf{f}'(u)(v - u)]\|_{0, \Omega} + \frac{1}{2} \|\mathbf{div} [\mathbf{f}''(w)(v - u)^2]\|_{0, \Omega}.$$

176 Notice that the second term in the right-hand side of (3.6) is a higher order term comparing to the
 177 first term. Now, the inequality in (3.5) is a direct consequence of the equality in (3.5) and (3.6).
 178 This completes the proof of the lemma. \square

179 REMARK 3.2. When u is sufficiently smooth, the second term

$$180 \quad \mathbf{div} [\mathbf{f}'(u)(v - u)] = (v - u) \mathbf{div} \mathbf{f}'(u) + \mathbf{f}'(u) \cdot \nabla(v - u)$$

181 may be bounded by the sum of the L^2 norms of $v - u$ and the directional derivative of $v - u$ along
 182 the direction $\mathbf{f}'(u)$.

183 Evaluation of the least-squares functional $\mathcal{L}(v; g)$ defined in (2.5) requires integration and
 184 differentiation over the computational domain and the inflow boundary. As in [9], we evaluate the
 185 integral of the least-squares functional by numerical integration. To do so, let

$$186 \quad \mathcal{T} = \{K : K \text{ is an open subdomain of } \Omega\} \quad \text{and} \quad \mathcal{E}_- = \{E = \partial K \cap \Gamma_- : K \in \mathcal{T}\}$$

187 be partitions of the domain Ω and the inflow boundary Γ_- , respectively. For each $K \in \mathcal{T}$ and
 188 $E \in \mathcal{E}_-$, let \mathcal{Q}_K and \mathcal{Q}_E be Newton-Cotes quadrature of integrals over K and E , respectively. The
 189 corresponding discrete least-squares functional is defined by

$$190 \quad (3.7) \quad \mathcal{L}_{\mathcal{T}}(v; g) = \sum_{K \in \mathcal{T}} \mathcal{Q}_K^2(\mathbf{div}_{\mathcal{T}} \mathbf{f}(v)) + \sum_{E \in \mathcal{E}_-} \mathcal{Q}_E^2(v - g),$$

191 where $\mathbf{div}_{\mathcal{T}}$ denotes a discrete divergence operator. The discrete divergence operators of the Roe
 192 and ENO type were studied in [6]. In the subsequent section, we will introduce new discrete
 193 divergence operators tailor to the LSNN method that are accurate approximations to the divergence
 194 operator when applying to discontinuous solution.

195 With the discrete least-squares functional $\mathcal{L}_{\mathcal{T}}(v; g)$, the least-squares neural network (LSNN)
 196 method is to find $u_{\mathcal{T}}^N(\mathbf{z}, \boldsymbol{\theta}^*) \in \mathcal{M}_N$ such that

$$197 \quad (3.8) \quad \mathcal{L}_{\mathcal{T}}(u_{\mathcal{T}}^N(\cdot, \boldsymbol{\theta}^*); g) = \min_{v \in \mathcal{M}_N} \mathcal{L}_{\mathcal{T}}(v(\cdot; \boldsymbol{\theta}); g) = \min_{\boldsymbol{\theta} \in \mathbb{R}^N} \mathcal{L}_{\mathcal{T}}(v(\cdot; \boldsymbol{\theta}); g).$$

198 LEMMA 3.3. Let u , u^N , and u_τ^N be the solutions of problems (2.5), (3.4), and (3.8), respectively.
 199 Then we have

$$200 \quad (3.9) \quad \mathcal{L}(u_\tau^N; g) \leq \left| (\mathcal{L} - \mathcal{L}_\tau)(u_\tau^N; g) \right| + \left| (\mathcal{L} - \mathcal{L}_\tau)(u^N; g) \right| + \left| \mathcal{L}(u^N; g) \right|.$$

201 *Proof.* By the fact that $\mathcal{L}_\tau(u_\tau^N; \mathbf{f}) \leq \mathcal{L}_\tau(u^N; \mathbf{f})$, we have

$$\begin{aligned} 202 \quad \mathcal{L}(u_\tau^N; g) &= (\mathcal{L} - \mathcal{L}_\tau)(u_\tau^N; g) + \mathcal{L}_\tau(u_\tau^N; g) \leq (\mathcal{L} - \mathcal{L}_\tau)(u_\tau^N; g) + \mathcal{L}_\tau(u^N; g) \\ 203 \quad (3.10) \quad &= (\mathcal{L} - \mathcal{L}_\tau)(u_\tau^N; g) + (\mathcal{L}_\tau - \mathcal{L})(u^N; g) + \mathcal{L}(u^N; g), \end{aligned}$$

204 which, together with the triangle inequality, implies (3.9). \square

205 This lemma indicates that the minimum of the discrete least-squares functional \mathcal{L}_τ over \mathcal{M}_N
 206 is bounded by the minimum of the least-squares functional \mathcal{L} over \mathcal{M}_N plus the approximation
 207 error of numerical integration and differentiation in \mathcal{M}_N .

208 In the remainder of this section, we describe the block space-time LSNN method introduced
 209 in [6] for dealing with the training difficulty over a relative large computational domain Ω . The
 210 method is based on a partition $\{\Omega_{k-1,k}\}_{k=1}^{n_b}$ of the computational domain Ω . To define $\Omega_{k-1,k}$, let
 211 $\{\Omega_k\}_{k=1}^{n_b}$ be subdomains of Ω satisfying the following inclusion relation

$$212 \quad \emptyset = \Omega_0 \subset \Omega_1 \subset \cdots \subset \Omega_{n_b} = \Omega.$$

213 Then set $\Omega_{k-1,k} = \Omega_k \setminus \Omega_{k-1}$ for $k = 1, \dots, n_b$. Assume that $\Omega_{k-1,k}$ is in the range of influence of

$$214 \quad \Gamma_{k-1,k} = \partial\Omega_{k-1,k} \cap \partial\Omega_{k-1} \quad \text{and} \quad \Gamma_-^k = \partial\Omega_{k-1,k} \cap \Gamma_-.$$

215 Denote by $u^k = u|_{\Omega_{k-1,k}}$ the restriction of the solution u of (2.2) on $\Omega_{k-1,k}$, then u^k is the
 216 solution of the following problem:

$$217 \quad (3.11) \quad \begin{cases} \mathbf{div}_\tau \mathbf{f}(u^k) = 0, & \text{in } \Omega_{k-1,k} \in \mathbb{R}^{d+1}, \\ u^k = u^{k-1}, & \text{on } \Gamma_{k-1,k}, \\ u^k = g, & \text{on } \Gamma_-^k. \end{cases}$$

218 Let

$$219 \quad \mathcal{L}^k(v; u^{k-1}, g) = \|\mathbf{div} \mathbf{f}(v)\|_{0, \Omega_{k-1,k}}^2 + \|v - u^{k-1}\|_{0, \Gamma_{k-1,k}}^2 + \|v - g\|_{0, \Gamma_-^k}^2,$$

220 and define the corresponding discrete least-squares functional $\mathcal{L}_\tau^k(v; u^{k-1}, g)$ over the subdomain
 221 $\Omega_{k-1,k}$ in a similar fashion as in (3.7). Now, the block space-time LSNN method is to find
 222 $u_\tau^k(\mathbf{z}, \boldsymbol{\theta}_k^*) \in \mathcal{M}_N$ such that

$$223 \quad (3.12) \quad \mathcal{L}_\tau^k(u_\tau^k(\cdot; \boldsymbol{\theta}_k^*); u^{k-1}, g) = \min_{v \in \mathcal{M}_N} \mathcal{L}_\tau^k(v(\cdot; \boldsymbol{\theta}); u^{k-1}, g) = \min_{\boldsymbol{\theta} \in \mathbb{R}^N} \mathcal{L}_\tau^k(v(\cdot; \boldsymbol{\theta}); u^{k-1}, g)$$

224 for $k = 1, \dots, n_b$.

225 **4. Discrete Divergence Operator.** As seen in [7, 6], numerical approximation of the dif-
 226 ferential operator is critical for the success of the LSNN method. Standard numerical or automatic
 227 differentiation along coordinate directions generally results in an inaccurate LSNN method, even
 228 for linear problems when solutions are discontinuous. This is because the differential form of the
 229 HCL is invalid at discontinuous interface. To overcome this difficulty, we used the discrete direc-
 230 tional differentiation for linear problems in [7] and the discrete divergence operator of the Roe and
 231 ENO type for nonlinear problems in [6].

232 In this section, we introduce a new discrete divergence operator based on the definition of
 233 the divergence operator. Specifically, for each $K \in \mathcal{T}$, let $\mathbf{z}_K^i = (\mathbf{x}_K^i, t_K^i)$ and ω_i for $i \in J$ be

234 the quadrature points and weights for the quadrature \mathcal{Q}_K , where J is the index set. Hence, the
 235 discrete least-squares functional becomes

$$236 \quad \mathcal{L}_\mathcal{T}(v; g) = \sum_{K \in \mathcal{T}} \left(\sum_{i \in J} \omega_i \mathbf{div}_\mathcal{T} \mathbf{f}(v(\mathbf{z}_K^i)) \right)^2 + \sum_{E \in \mathcal{E}_-} \mathcal{Q}_E^2(v - g).$$

237 To define the discrete divergence operator $\mathbf{div}_\mathcal{T}$, we first construct a set of control volumes

$$238 \quad \mathcal{V} = \{V : V \text{ is an open subdomain of } \Omega\}$$

239 such that \mathcal{V} is a partition of the domain Ω and that each quadrature point is the centroid of a
 240 control volume $V \in \mathcal{V}$. Denote by V_K^i the control volume corresponding to the quadrature point
 241 \mathbf{z}_K^i , by the definition of the divergence operator, we have

$$242 \quad (4.1) \quad \mathbf{div} \mathbf{f}(u(\mathbf{z}_K^i)) \approx \text{avg}_{V_K^i} \mathbf{div} \mathbf{f}(u) = \frac{1}{|V_K^i|} \int_{\partial V_K^i} \mathbf{f}(u) \cdot \mathbf{n} \, dS,$$

243 where the average of a function φ over V_K^i is defined by

$$244 \quad \text{avg}_{V_K^i} \varphi = \frac{1}{|V_K^i|} \int_{V_K^i} \varphi(\mathbf{z}) \, d\mathbf{z}.$$

245 The average of φ with respect to the partition \mathcal{V} is denoted by $\text{avg}_\mathcal{V} \varphi$ and defined as a piece-wise
 246 constant function through its restriction on each $V \in \mathcal{V}$ by

$$247 \quad \text{avg}_\mathcal{V} \varphi|_V = \text{avg}_V \varphi.$$

248 Now we may design a discrete divergence operator $\mathbf{div}_\mathcal{T}$ acting on the total flux $\mathbf{f}(u)$ by approxi-
 249 mating the surface integral on the right-hand side of (4.1).

250 All existing conservative schemes of various order such as Roe, ENO, WENO, etc. may be
 251 viewed as approximations of the surface integral using values of $\mathbf{f}(u)$ at some *mesh points*, where
 252 most of them are outside of \bar{V} . These conservative schemes are nonlinear methods because the
 253 procedure determining proper mesh points to be used for approximating the average of the spatial
 254 flux is a nonlinear process due to possible discontinuity.

255 Because the LSNN method is a “mesh/point-less” space-time method, all points on $\partial V \in \mathbb{R}^{d+1}$
 256 are at our disposal for approximating the surface integral. Hence, the surface integral can be
 257 approximated as accurately as desired by using only points on ∂V . When u and hence $f_i(u)$ are
 258 discontinuous on ∂V , the best linear approximation strategy is to use piece-wise constant/linear
 259 functions on a sufficiently fine partition of each face of ∂V , instead of higher order polynomials on
 260 each face. This suggests that a composite lower-order numerical integration such as the composite
 261 mid-point/trapezoidal quadrature would provide accurate approximation to the surface integral
 262 in (4.1), and hence the resulting discrete divergence operator would be accurate approximation to
 263 the divergence operator, even if the solution is discontinuous.

264 **4.1. One Dimension.** For clarity of presentation, the discrete divergence operator described
 265 above will be first introduced in this section in one dimension. To this end, to approximate single
 266 integral $I(\varphi) = \int_c^d \varphi(s) \, ds$, we will use the composite midpoint/trapezoidal rule:

$$267 \quad (4.2) \quad Q(\varphi(s); c, d, p) = \begin{cases} \frac{d-c}{p} \sum_{i=0}^{p-1} \varphi(s_{i+1/2}), & \text{midpoint,} \\ \frac{d-c}{2p} \left(\varphi(c) + \varphi(d) + 2 \sum_{i=1}^{p-1} \varphi(s_i) \right), & \text{trapezoidal,} \end{cases}$$

268 where $\{s_i\}_{i=0}^p$ uniformly partitions the interval $[c, d]$ into p sub-intervals.

269 Let $\Omega = (a, b) \times (0, T)$. For simplicity, assume that the integration partition \mathcal{T} introduced in
270 Section 3 is a uniform partition of the domain Ω ; i.e.,

$$271 \quad \mathcal{T} = \{K = K_{ij} : i = 0, 1, \dots, m-1; j = 0, 1, \dots, n-1\} \text{ with } K_{ij} = (x_i, x_{i+1}) \times (t_j, t_{j+1}),$$

272 where $x_i = a + ih$ and $t_j = j\tau$ with $h = (b-a)/m$ and $\delta = T/n$. For integration subdomain K_{ij} ,
273 the set of quadrature points is

$$\begin{aligned} 274 \quad M_{ij} &= \{\mathbf{z}_{i+\frac{1}{2}, j+\frac{1}{2}}\} && \text{for the midpoint rule,} \\ T_{ij} &= \{\mathbf{z}_{i,j}, \mathbf{z}_{i+1,j}, \mathbf{z}_{i,j+1}, \mathbf{z}_{i+1,j+1}\} && \text{for the trapezoidal rule,} \\ \text{and } S_{ij} &= M_{ij} \cup T_{ij} \cup \{\mathbf{z}_{i+\frac{1}{2}, j}, \mathbf{z}_{i,j+\frac{1}{2}}, \mathbf{z}_{i+1, j+\frac{1}{2}}, \mathbf{z}_{i+\frac{1}{2}, j+1}\} && \text{for the Simpson rule,} \end{aligned}$$

275 where $\mathbf{z}_{i+k, j+l} = (x_i + kh, t_j + l\delta)$ for $k, l = 0, 1/2$, or 1 . Based on those quadrature points, the
276 sets of control volumes may be defined accordingly. For example, the control volume \mathcal{V}_m for the
277 midpoint rule is \mathcal{T} ; the control volume \mathcal{V}_t for the trapezoidal rule is obtained by shifting control
278 volumes in \mathcal{V}_m by $\frac{1}{2}(h, \delta)$ plus half-size control volumes along the boundary; and the control
279 volume \mathcal{V}_s for the Simpson rule is obtained in a similar fashion as \mathcal{V}_t on the element size of $h/2$
280 and $\delta/2$ for space and time, respectively.

281 For simplicity of presentation, we define the discrete divergence operator only for the midpoint
282 rule for it can be defined in a similar fashion for other quadrature. Since $\mathcal{V}_m = \mathcal{T}$, i.e., the control
283 volume of \mathcal{V}_m is the same as the element of \mathcal{T} , for each control volume $V = K_{ij}$, denote its centroid
284 by

$$285 \quad \mathbf{z}_V = \mathbf{z}_{ij} = (x_i + h/2, t_j + \delta/2).$$

286 Denote by $\sigma = f(u)$ the spatial flux, then the total flux is the two-dimensional vector field $\mathbf{f}(u) =$
287 (σ, u) . Denote the first-order finite difference quotients by

$$288 \quad \sigma(x_i, x_{i+1}; t) = \frac{\sigma(x_{i+1}, t) - \sigma(x_i, t)}{x_{i+1} - x_i} \quad \text{and} \quad u(x; t_j, t_{j+1}) = \frac{u(x, t_{j+1}) - u(x, t_j)}{t_{j+1} - t_j}.$$

289 Then the surface integral in (4.1) becomes

$$290 \quad (4.3) \quad \frac{1}{|K_{ij}|} \int_{\partial K_{ij}} \mathbf{f}(u) \cdot \mathbf{n} dS = \delta^{-1} \int_{t_j}^{t_{j+1}} \sigma(x_i, x_{i+1}; t) dt + h^{-1} \int_{x_i}^{x_{i+1}} u(x; t_j, t_{j+1}) dx.$$

291 Approximating single integrals by the composite midpoint/trapezoidal rule, we obtain the following
292 discrete divergence operator

$$293 \quad (4.4) \quad \mathbf{div}_\tau \mathbf{f}(u(\mathbf{z}_{ij})) = \delta^{-1} Q(\sigma(x_i, x_{i+1}; t); t_j, t_{j+1}, \hat{n}) + h^{-1} Q(u(x; t_j, t_{j+1}); x_i, x_{i+1}, \hat{m}).$$

294 **REMARK 4.1.** Denote by $u_{i,j}$ as approximation to $u(x_i, t_j)$. (4.4) with $\hat{m} = \hat{n} = 1$ using the
295 trapezoidal rule leads to the following implicit conservative scheme for the one-dimensional scalar
296 nonlinear HCL:

$$297 \quad (4.5) \quad \frac{u_{i+1, j+1} + u_{i, j+1}}{\delta} + \frac{f(u_{i+1, j+1}) - f(u_{i, j+1})}{h} = \frac{u_{i+1, j} + u_{i, j}}{\delta} - \frac{f(u_{i+1, j}) - f(u_{i, j})}{h}$$

298 for $i = 0, 1, \dots, m-1$ and $j = 0, 1, \dots, n-1$.

299 Below, we state error estimates of the discrete divergence operator defined in (4.4) and post-
300 pone their proof to Appendix.

301 LEMMA 4.2. For any $K_{ij} \in \mathcal{T}$, assume that u is a C^2 function on every edge of the rectangle
 302 ∂K_{ij} . Then there exists a constant $C > 0$ such that

$$303 \quad \|\mathbf{div}_\tau \mathbf{f}(u) - \text{avg}_\tau \mathbf{div} \mathbf{f}(u)\|_{L^p(K_{ij})}$$

$$304 \quad (4.6) \quad \leq C \left(\frac{h^{1/p} \delta^2}{\hat{n}^2} \|\sigma_{tt}(x_{i+1}, x_i; \cdot)\|_{L^p(t_j, t_{j+1})} + \frac{h^2 \delta^{1/p}}{\hat{m}^2} \|u_{xx}(\cdot; t_{j+1}, t_j)\|_{L^p(x_i, x_{i+1})} \right).$$

305 This lemma indicates that $\hat{m} = 1$ and $\hat{n} = 1$ are sufficient if the solution is smooth on
 306 ∂K_{ij} . In this case, we may use higher order numerical integration, e.g., the Gauss quadrature,
 307 to approximate the surface integral in (4.3) for constructing a higher order discrete divergence
 308 operator.

309 When u is discontinuous on ∂K_{ij} , error estimate on the discrete divergence operator becomes
 310 more involved. To this end, first we consider the case that the discontinuous interface Γ_{ij} (a straight
 311 line) intersects two horizontal boundary edges of K_{ij} . Denote by $u_{ij} = u|_{K_{ij}}$ the restriction of u
 312 in K_{ij} and by $\llbracket u_{ij} \rrbracket_{t_l}$ the jump of u_{ij} on the horizontal boundary edge $t = t_l$ of K_{ij} , where $l = j$
 313 and $l = j + 1$.

314 LEMMA 4.3. Assume that u is a C^2 function of t and a piece-wise C^2 function of x on two
 315 vertical and two horizontal edges of K_{ij} , respectively. Moreover, u has only one discontinuous
 316 point on each horizontal edge. Then there exists a constant $C > 0$ such that

$$317 \quad \|\mathbf{div}_\tau \mathbf{f}(u) - \text{avg}_\tau \mathbf{div} \mathbf{f}(u)\|_{L^p(K_{ij})}$$

$$318 \quad (4.7) \quad \leq C \left(\frac{h^{1/p} \delta^2}{\hat{n}^2} + \frac{h^2 \delta^{1/p}}{\hat{m}^2} + \frac{h \delta^{1/p}}{\hat{m}^{1+1/q}} \right) + \frac{(h\delta)^{1/p}}{\hat{m}} \sum_{l=j}^{j+1} \llbracket u_{ij} \rrbracket_{t_l}.$$

319 REMARK 4.4. Lemma 4.3 implies that the choice of the number of sub-intervals of (x_i, x_{i+1})
 320 on the composite numerical integration depends on the size of the jump of the solution and that
 321 large \hat{m} would guarantee accuracy of the discrete divergence operator when u is discontinuous on
 322 ∂K_{ij} .

323 REMARK 4.5. Error bounds similar to (4.7) hold for the other cases: Γ_{ij} intercepts (i) two
 324 vertical edges or (ii) one horizontal and one vertical edges of K_{ij} . Specifically, we have

$$325 \quad \|\mathbf{div}_\tau \mathbf{f}(u) - \text{avg}_\tau \mathbf{div} \mathbf{f}(u)\|_{L^p(K_{ij})} \leq C \left(\frac{h^{1/p} \delta^2}{\hat{n}^2} + \frac{h^2 \delta^{1/p}}{\hat{m}^2} + \frac{h^{1/p} \delta}{\hat{n}^{1+1/q}} \right) + \frac{(h\delta)^{1/p}}{\hat{n}} \sum_{l=i}^{i+1} \llbracket \sigma_{ij} \rrbracket_{x_l}$$

326 for the case (i) and

$$327 \quad \|\mathbf{div}_\tau \mathbf{f}(u) - \text{avg}_\tau \mathbf{div} \mathbf{f}(u)\|_{L^p(K_{ij})} \leq C \left(\frac{h^{1/p} \delta^2}{\hat{n}^2} + \frac{h^2 \delta^{1/p}}{\hat{m}^2} + \frac{h \delta^{1/p}}{\hat{m}^{1+1/q}} + \frac{h^{1/p} \delta}{\hat{n}^{1+1/q}} \right) + E_{ij}$$

328 for the case (ii), where $E_{ij} = (h\delta)^{1/p} \left(\frac{1}{\hat{m}} \llbracket u_{ij} \rrbracket_{t_l} + \frac{1}{\hat{n}} \llbracket \sigma_{ij} \rrbracket_{x_l} \right)$ with $x_l = x_i$ or x_{i+1} and $t_l = t_j$ or
 329 t_{j+1} .

330 **4.2. Two Dimensions.** This section describes the discrete divergence operator in two di-
 331 mensions. As in one dimension, the discrete divergence operator is defined as an approximation to
 332 the average of the divergence operator through the composite mid-point/trapezoidal quadrature
 333 to approximate the surface integral (4.1). Extension to three dimensions is straightforward.

334 To this end, we first describe the composite mid-point/trapezoidal numerical integration for
 335 approximating a double integral over a rectangle region $T = (c_1, d_1) \times (c_2, d_2)$

$$336 \quad I(\varphi) = \int_T \varphi(s_1, s_2) ds_1 ds_2$$

$$337 \quad \approx Q(\varphi(s_1, s_2); c_1, d_1, p_1; c_2, d_2, p_2) \equiv Q\left(Q(\varphi(s_1, \cdot); c_1, d_1, p_1)(s_2); c_2, d_2, p_2\right),$$

338 where $Q(\varphi(s_1, \cdot); c_1, d_1, p_1)$ is the composite quadrature defined in (4.2).

339 For simplicity, let $\Omega = \tilde{\Omega} \times I = (a_1, b_1) \times (a_2, b_2) \times (0, T)$, and assume that the integration
 340 partition \mathcal{T} introduced in Section 3 is a uniform partition of the domain Ω ; i.e.,

$$341 \quad \mathcal{T} = \{K = K_{ijk} : i = 0, 1, \dots, m_1 - 1; j = 0, 1, \dots, m_2 - 1; k = 0, 1, \dots, n - 1\}$$

342 with $K_{ijk} = (x_i, x_{i+1}) \times (y_j, y_{j+1}) \times (t_k, t_{k+1})$, where

$$343 \quad x_i = a_1 + ih_1, \quad y_j = a_2 + jh_2, \quad \text{and} \quad t_k = k\delta,$$

344 and $h_l = (b_l - a_l)/m_l$ for $l = 1, 2$ and $\delta = T/n$ are the respective spatial and temporal sizes of
 345 the integration mesh. Again, we define the discrete divergence operator only corresponding to the
 346 midpoint rule. Denote the mid-point of K_{ijk} by

$$347 \quad \mathbf{z}_{ijk} = \left(x_i + \frac{h_1}{2}, y_j + \frac{h_2}{2}, t_k + \frac{\delta}{2}\right).$$

348 Let $\boldsymbol{\sigma} = (\sigma_1, \sigma_2) = (f_1(u), f_2(u))$, then the space-time flux is the three-dimensional vector
 349 field: $\mathbf{f}(u) = (\boldsymbol{\sigma}, u) = (\sigma_1, \sigma_2, u)$. Denote the the first-order finite difference quotients by

$$350 \quad \sigma_1(y, t; x_i, x_{i+1}) = \frac{\sigma_1(x_{i+1}, y, t) - \sigma_1(x_i, y, t)}{x_{i+1} - x_i}, \quad \sigma_2(x, t; y_j, y_{j+1}) = \frac{\sigma_2(x, y_{j+1}, t) - \sigma_2(x, y_j, t)}{y_{j+1} - y_j},$$

$$351 \quad \text{and} \quad u(x, y; t_k, t_{k+1}) = \frac{u(x, y, t_{k+1}) - u(x, y, t_k)}{t_{k+1} - t_k}.$$

352 Denote three faces of ∂K_{ijk} by

$$353 \quad K_{ij}^{xy} = (x_i, x_{i+1}) \times (y_j, y_{j+1}), \quad K_{ik}^{xt} = (x_i, x_{i+1}) \times (t_k, t_{k+1}), \quad \text{and} \quad K_{jk}^{yt} = (y_j, y_{j+1}) \times (t_k, t_{k+1}).$$

354 Then the surface integral in (4.1) becomes

$$355 \quad \frac{1}{|K_{ijk}|} \int_{\partial K_{ijk}} \mathbf{f}(u) \cdot \mathbf{n} dS = (h_2\delta)^{-1} \int_{K_{jk}^{yt}} \sigma_1(y, t; x_{i+1}, x_i) dydt$$

$$356 \quad (4.8) \quad + (h_1\delta)^{-1} \int_{K_{ik}^{xt}} \sigma_2(x, t; y_{j+1}, y_j) dxdt + (h_1h_2)^{-1} \int_{K_{ij}^{xy}} u(x, y; t_{k+1}, t_k) dx dy.$$

357 Approximating double integrals by the composite midpoint/trapezoidal rule, we obtain the follow-
 358 ing discrete divergence operator

$$359 \quad \mathbf{div}_\tau \mathbf{f}(u(\mathbf{z}_{ijk})) = (h_2\delta)^{-1} Q(\sigma_1(y, t; x_{i+1}, x_i); y_j, y_{j+1}, \hat{m}_2; t_k, t_{k+1}, \hat{n})$$

$$360 \quad + (h_1\delta)^{-1} Q(\sigma_2(x, t; y_{j+1}, y_j); x_i, x_{i+1}, \hat{m}_1; t_k, t_{k+1}, \hat{n})$$

$$361 \quad (4.9) \quad + (h_1h_2)^{-1} Q(u(x, y; t_{k+1}, t_k); x_i, x_{i+1}, \hat{m}_1; y_j, y_{j+1}, \hat{m}_2).$$

362 **4.3. Integration mesh size.** The discrete divergence operator defined in (4.4) and (4.9) for
 363 the respective one- and two- dimension is based on the composite midpoint/trapezoidal rule. As
 364 shown in Lemmas 4.2 and 4.3 and Remark 4.5, the discrete divergence operator can be as accurate
 365 as desired for the discontinuous solution provided that the size of integration mesh is sufficiently
 366 small.

367 To reduce computational cost, note that the discontinuous interfaces of the solution u lie on
 368 d -dimensional hyper-planes. Hence, they only intersect with a small portion of control volumes
 369 in \mathcal{T} . This observation suggests that sufficiently fine meshes are only needed for control volumes
 370 at where the solution is possibly discontinuous. To realize this idea, we divide the set of control
 371 volumes into two subsets:

$$372 \quad \mathcal{T} = \mathcal{T}_c \cup \mathcal{T}_d,$$

373 where the solution u is continuous in each control volume of \mathcal{K}_c^l and possibly discontinuous at some
 374 control volumes of \mathcal{T}_d ; i.e.,

$$375 \quad \mathcal{T}_c = \{K \in \mathcal{T} : u \in C(K)\} \quad \text{and} \quad \mathcal{T}_d = \mathcal{T} \setminus \mathcal{T}_c.$$

376 Next, we describe how to determine the set of control volumes \mathcal{T}_d in one dimension by the range
 377 of influence. It is well-known that characteristic curves are straight lines before their interception
 378 and are given by

$$379 \quad (4.10) \quad x = x(T_l) + (t - T_l) f'(u(x(T_l), T_l)).$$

380 For $i = 0, 1, \dots, m$, let

$$381 \quad \hat{x}_i = x_i + (T_{l+1} - T_l) f'(u_N^l(x_i, T_l)),$$

382 where $u_N^l(x_i, T_l)$ is the neural network approximation from the previous time block

$$383 \quad \Omega \times I_{l-1} = (a, b) \times (T_{l-1}, T_l).$$

384 Clearly, the solution u is discontinuous in a control volume $V_i \times I_l^k$ if either (1) $u(x, T_l)$ is
 385 discontinuous at the interval V_i or (2) there are two characteristic lines intercepting in $V_i \times I_l^k$. In
 386 the first case, $V_i \times I_l^k$ is in \mathcal{K}_d^l if $u_N^l(x, T_l)$ has a sharp change in the interval V_i ; moreover, either
 387 $V_{i-1} \times I_l^k \in \mathcal{K}_d^l$ if $\hat{x}_i < x_i$ or $V_{i+1} \times I_l^k \in \mathcal{K}_d^l$ if $\hat{x}_{i+1} > x_{i+1}$. In the second case, assume that
 388 $\hat{x}_i > \hat{x}_{i+1}$, then $V_i \times I_l^k \in \mathcal{K}_d^l$ if $\hat{x}_i < x_{i+1}$.

389 **5. Numerical Experiments.** This section presents numerical results of the block space-time
 390 LSNN method for one and two dimensional problems. Let $\Omega = \tilde{\Omega} \times (0, T)$. The k^{th} space-time
 391 block is defined as

$$392 \quad \Omega_{k-1,k} = \Omega_k \setminus \Omega_{k-1} = \tilde{\Omega} \times \left(\frac{(k-1)T}{n_b}, \frac{kT}{n_b} \right) \quad \text{for } k = 1, \dots, n_b,$$

393 where $\Omega_k = \tilde{\Omega} \times (0, kT/n_b)$. For efficient training, the least-squares functional is modified as
 394 follows:

$$395 \quad (5.1) \quad \mathcal{L}^k(v; u^{k-1}, g) = \|\mathbf{div} \mathbf{f}(v)\|_{0, \Omega_{k-1,k}}^2 + \alpha (\|v - u^{k-1}\|_{0, \Gamma_{k-1,k}}^2 + \|v - g\|_{0, \Gamma_k^-}^2),$$

396 where α is a weight to be chosen empirically.

397 Unless otherwise stated, the integration mesh \mathcal{T}_k is a uniform partition of $\Omega_{k-1,k}$ with $h = \delta =$
 398 0.01, and the discrete divergence operator defined in (4.4) is based on the composite trapezoidal
 399 rule with $\hat{m} = \hat{n} = 2$. Three-layer or four-layer neural network are employed for all test problems
 400 and are denoted by $d_i n - n_1 - n_2 (-n_3) - 1$ with n_1, n_2 and n_3 neurons in the respective first, second and
 401 third (for a four-layer NN) layers. The same network structure is used for all time blocks.

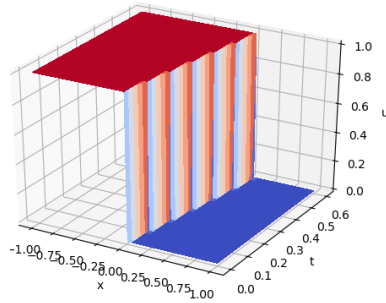
402 The network is trained by using the ADAM [24] (a variant of the method of gradient descent)
 403 with either a fixed or an adaptive learning rate to iteratively solve the minimization problem in
 404 (3.12). Parameters of the first block is initialized by an approach introduced in [27], and those for
 405 the current block is initialized by using the NN approximation of the previous block (see Remark
 406 4.1 of [6]).

407 The solution of the problem in (3.11) and its corresponding NN approximation are denoted by
 408 u^k and $u_{\mathcal{T}}^k$, respectively. Their traces are depicted on a plane of given time and exhibit capability
 409 of the numerical approximation in capturing shock/rarefaction.

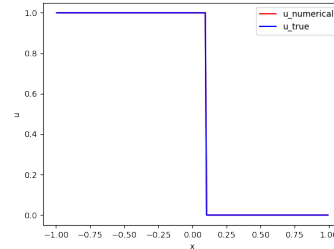
410 **5.1. Inviscid Burgers' equation.** This section reports numerical results of the block space-
 411 time LSNN method for the one dimensional inviscid Burgers equation, where the spatial flux is
 412 $\tilde{f}(u) = f(u) = \frac{1}{2}u^2$.

TABLE 1
 Relative L^2 errors of Riemann problem (shock) for Burgers' equation

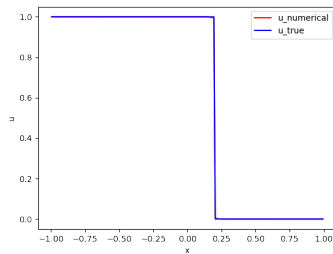
Network structure	Block	$\frac{\ u^k - u_{\mathcal{T}}^k\ _0}{\ u^k\ _0}$
2-10-10-1	$\Omega_{0,1}$	0.048774
	$\Omega_{1,2}$	0.046521
	$\Omega_{2,3}$	0.044616



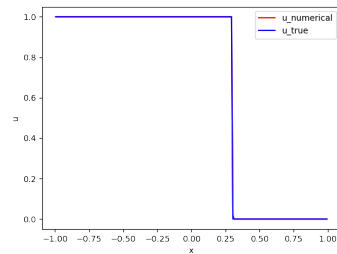
(a) Exact solution u on Ω



(b) Traces at $t = 0.2$



(c) Traces at $t = 0.4$



(d) Traces at $t = 0.6$

FIG. 1. Approximation results of Riemann problem (shock) for Burgers' equation

413 The first two test problems are the Riemann problem with the initial condition: $u_0(x) =$
 414 $u(x, 0) = u_L$ if $x \leq 0$ or u_R if $x \geq 0$.

415 **Shock formation.** When $u_L = 1 > 0 = u_R$, a shock is formed immediately with the shock speed
 416 $s = (u_L + u_R)/2$. The first test problem is defined on a computational domain $\Omega = (-1, 1) \times (0, 0.6)$

417 with inflow boundary

$$418 \quad \Gamma_- = \Gamma_-^L \cup \Gamma_-^R \equiv \{(-1, t) : t \in [0, 0.6]\} \cup \{(1, t) : t \in [0, 0.6]\}$$

419 and boundary conditions: $g = u_L = 1$ on Γ_-^L and $g = u_R = 0$ on Γ_-^R . With $n_b = 3$ blocks, weight
 420 $\alpha = 20$, a fixed learning rate 0.003, and 30000 iterations for each block, the relative errors in the
 421 L^2 norm are reported in Table 1. Traces of the exact solution and numerical approximation on the
 422 planes $t = kT/n_b$ for $k = 1, 2, 3$ are depicted in Fig. 1(b)-(d), which clearly indicate that the LSNN
 423 method is capable of capturing the shock formation and its speed. Moreover, it approximates the
 424 solution well without oscillations.

TABLE 2
 Relative L^2 errors of Riemann problem (rarefaction) for Burgers' equation

Network structure	Block	$\frac{\ u^k - u_\tau^k\ _0}{\ u^k\ _0}$
2-10-10-1	$\Omega_{0,1}$	0.013387
	$\Omega_{1,2}$	0.010079

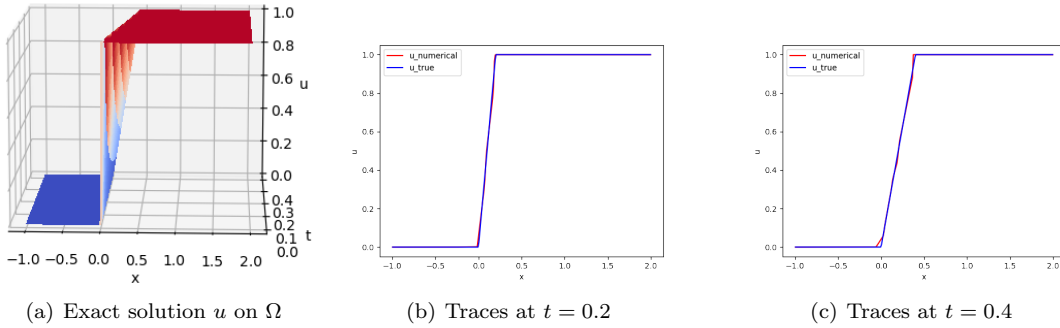


FIG. 2. Approximation results of Riemann problem (rarefaction) for Burgers' equation

425 **Rarefaction waves.** When $u_L = 0 < 1 = u_R$, the range of influence of all points in \mathbb{R} is a proper
 426 subset of $\mathbb{R} \times [0, \infty)$. Hence, the weak solution of the scalar hyperbolic conservation law is not
 427 unique. The second test problem is defined on a computational domain $\Omega = (-1, 2) \times (0, 0.4)$ with
 428 inflow boundary condition $g = 0$ on $\Gamma_- = \{(-1, t) : t \in [0, 0.4]\}$. As shown in Section 5.1.2 of
 429 [6], the LSNN method using Roe's scheme has a limitation to resolve the rarefaction. Numerical
 430 results of the LSNN method using the discrete divergence operator ($n_b = 2$, $\alpha = 10$, a fixed
 431 learning rate 0.003, and 40000 iterations) are reported in Table 2. Traces of the exact solution
 432 and numerical approximation on the planes $t = 0.2$ and $t = 0.4$ are depicted in Fig. 2. This test
 433 problem shows that the LSNN method using the \mathbf{div}_τ is able to compute the physically relevant
 434 vanishing viscosity solution (see, e.g., [25, 35]) without special treatment. This is possibly due to
 435 the fact that the LSNN approximation is continuous.

436 **Sinusoidal initial condition.** The third test problem has smooth initial condition $u_0(x) =$
 437 $0.5 + \sin(\pi x)$ and is defined on the computational domain $\Omega = (0, 2) \times (0, 0.8)$ with inflow boundary

$$438 \quad \Gamma_- = \Gamma_-^L \cup \Gamma_-^R \equiv \{(0, t) : t \in [0, 0.8]\} \cup \{(2, t) : t \in [0, 0.8]\}.$$

439 The shock of the problem appears at $t = 1/\pi \approx 0.318$. This is the same test problem as in Sec-
 440 tion 5.2 of [6] (see also [23, 36]). The goal of this experiment is to compare numerical performances
 441 of the LSNN methods using the \mathbf{div}_τ introduced in this paper and the ENO scheme in [6].

442 Since the solution of this problem is implicitly given, to accurately measure the quality of NN
 443 approximations, a benchmark reference solution \hat{u} is generated using the traditional mesh-based
 444 method. In particular, the third-order accurate WENO scheme [32] and the fourth-order Runge-
 445 Kutta method are employed for the respective spatial and temporal discretizations with a fine
 446 mesh ($\Delta x = 0.001$ and $\Delta t = 0.0002$) on the computational domain Ω .

447 The LSNN using \mathbf{div}_τ is implemented with the same set of hyper parameters as in Section 5.2
 448 of [6], i.e., training weight $\alpha = 5$ and an adaptive learning rate which starts with 0.005 and reduces
 449 by half for every 25000 iterations. Setting $n_b = 16$ and on each time block, the total number of
 450 iterations is set as 50000 and the size of the NN model is 2-30-30-1. Although we observe some error
 451 accumulation when the block evolves for both the LSNN methods, the one using \mathbf{div}_τ performs
 452 better than that using ENO (see Table 3 for the relative L^2 norm error and Fig. 3(a)-(h) for graphs
 453 near the left side of the interface).

TABLE 3
 Relative L^2 errors of Burgers' equation with a sinusoidal initial condition

Network structure	Block	LSNN using \mathbf{div}_τ	LSNN using ENO [6]
		$\frac{\ u^k - u_\tau^k\ _0}{\ u^k\ _0}$	$\frac{\ u^k - u_\tau^k\ _0}{\ u^k\ _0}$
2-30-30-1	$\Omega_{0,1}$	0.010641	0.010461
	$\Omega_{1,2}$	0.011385	0.012517
	$\Omega_{2,3}$	0.012541	0.019772
	$\Omega_{3,4}$	0.014351	0.022574
	$\Omega_{4,5}$	0.016446	0.029011
	$\Omega_{5,6}$	0.018634	0.038852
	$\Omega_{6,7}$	0.031103	0.075888
	$\Omega_{7,8}$	0.053114	0.078581
	$\Omega_{8,9}$	0.053562	—
	$\Omega_{9,10}$	0.064933	—
	$\Omega_{10,11}$	0.061354	—
	$\Omega_{11,12}$	0.077982	—
	$\Omega_{12,13}$	0.061145	—
	$\Omega_{13,14}$	0.070554	—
	$\Omega_{14,15}$	0.068539	—
	$\Omega_{15,16}$	0.065816	—

TABLE 4
 Relative L^2 errors of the problem with $f(u) = \frac{1}{4}u^4$ using the composite trapezoidal rule (4.2)

Time block	Number of sub-intervals		
	$\hat{m} = \hat{n} = 2$	$\hat{m} = \hat{n} = 4$	$\hat{m} = \hat{n} = 6$
$\Omega_{0,1}$	0.067712	0.010446	0.004543
$\Omega_{1,2}$	0.108611	0.008275	0.009613

454 **5.2. Riemann problem with $f(u) = \frac{1}{4}u^4$.** The goals of this set of numerical experi-
 455 ments are twofold. First, we compare the performance of the LSNN method using the com-
 456 posite trapezoidal/mid-point rule in (4.2). Second, we investigate the impact of the number of
 457 sub-intervals of the composite quadrature rule on the accuracy of the LSNN method.

458 The test problem is the Riemann problem with a convex flux $\mathbf{f}(u) = (f(u), u) = (\frac{1}{4}u^4, u)$
 459 and the initial condition $u_L = 1 > 0 = u_R$. The computational domain is chosen to be $\Omega =$

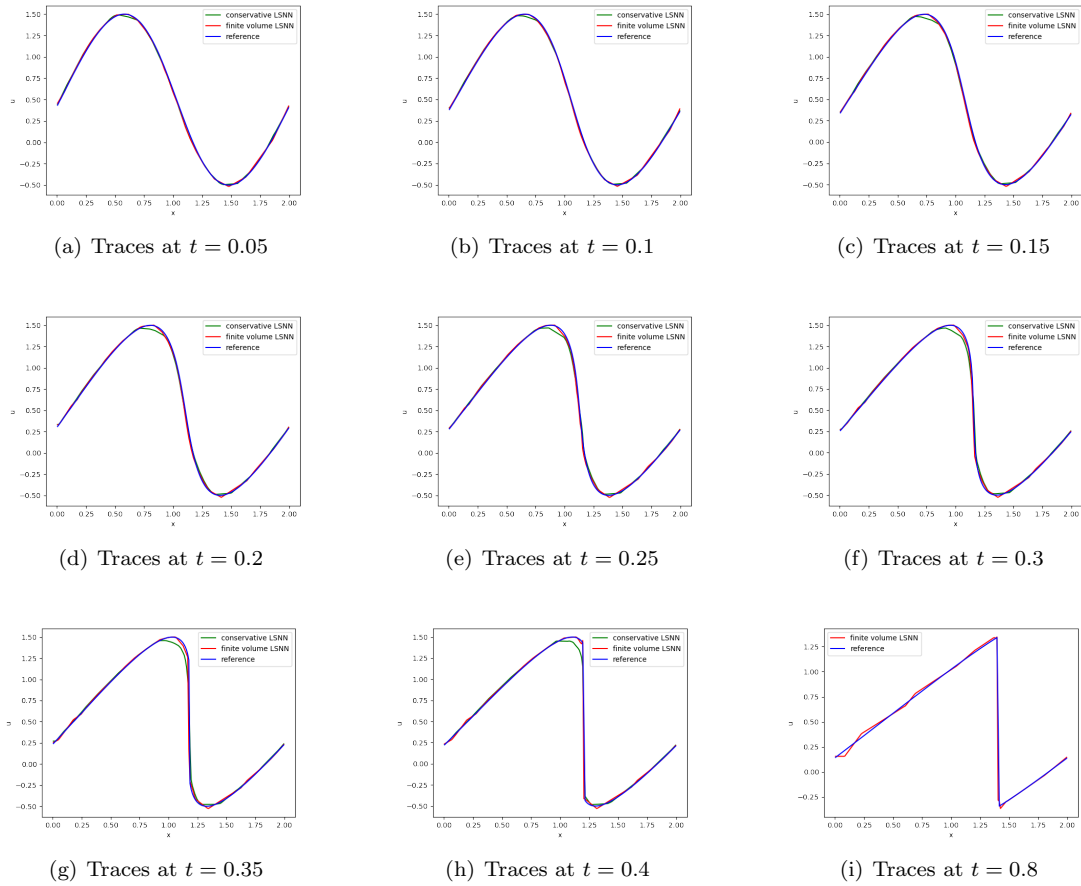


FIG. 3. Approximation results of Burgers' equation with a sinusoidal initial condition

TABLE 5
Relative L^2 errors of the problem with $f(u) = \frac{1}{4}u^4$ using the composite mid-point rule (4.2)

Time block	Number of sub-intervals		
	$\hat{m} = \hat{n} = 2$	$\hat{m} = \hat{n} = 4$	$\hat{m} = \hat{n} = 6$
$\Omega_{0,1}$	0.096238	0.007917	0.003381
$\Omega_{1,2}$	0.159651	0.007169	0.005028

460 $(-1, 1) \times (0, 0.4)$. Relative L^2 errors of the LSNN method using the \mathbf{div}_τ (2-10-10-1 NN model,
 461 $n_b = 2$, $\alpha = 20$, a fixed learning rate 0.003 for the first 30000 iterations and 0.001 for the remaining)
 462 are reported in Tables 4 and 5; and traces of the exact and numerical solutions are depicted in
 463 Fig. 4.

464 Clearly, Tables 4 and 5 indicate that the accuracy of the LSNN method depends on the
 465 number of sub-intervals (\hat{m} and \hat{n}) for the composite quadrature rule; i.e., the larger \hat{m} and \hat{n} are,
 466 the more accurate the LSNN method is. Moreover, the accuracy using the composite trapezoidal
 467 and mid-point rules in the LSNN method is comparable.

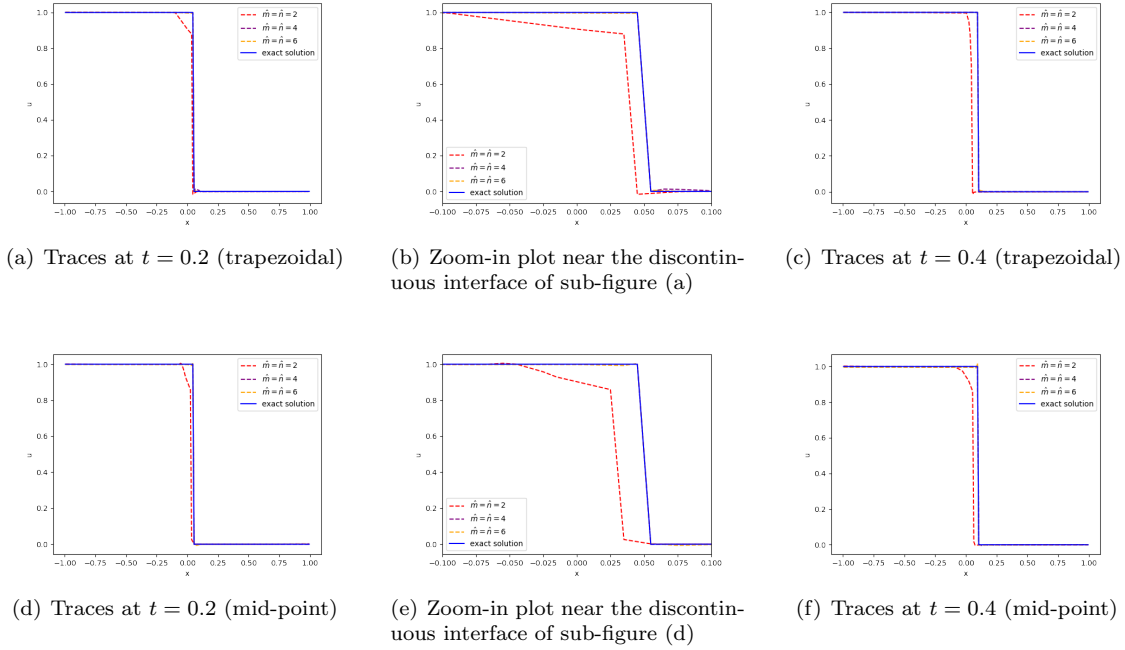


FIG. 4. Numerical results of the problem with $f(u) = \frac{1}{4}u^4$ using the composite trapezoidal and mid-point rules

TABLE 6
Relative L^2 errors of Riemann problem with a non-convex flux $f(u) = \frac{1}{3}u^3$

Network structure	Block	$\frac{\ u^k - u_{\mathcal{T}}^k\ _0}{\ u^k\ _0}$
2-64-64-64-1	$\Omega_{0,1}$	0.03277
	$\Omega_{1,2}$	0.03370
	$\Omega_{2,3}$	0.03450
	$\Omega_{3,4}$	0.03578

468 **5.3. Riemann problem with non-convex fluxes.** The test problem for a non-convex flux
 469 is a modification of the test problem in Section 5.2 by replacing the flux with $f(u) = \frac{1}{3}u^3$ and the
 470 initial condition with $u_L = 1 > -1 = u_R$. The Riemann solution consists partly of a rarefaction
 471 wave together with a shock wave which brings a new level of challenge with a compound wave.
 472 The exact solution is obtained through Osher's formulation [28] which has a shock speed $s=0.25$
 473 and a shock jump from 1 to -0.5 when $t > 0$.

474 The block space-time LSNN method using the $\mathbf{div}_{\mathcal{T}}$ with $\hat{m} = \hat{n} = 4$ is utilized for this
 475 problem. Four time blocks are computed on the temporal domain $(0, 0.4)$ and a relative larger
 476 network structure (2-64-64-64-1) is tested with a smaller integration mesh size $h = \delta = 0.005$
 477 to compute the compound wave more precisely. We tune the hyper parameter $\alpha = 200$, and
 478 all time blocks are computed with a total of 60000 iterations (learning rate starts with $1e-3$ and
 479 decay to 20% every 20000 iterations). Due to the random initial guess for the second hidden layer
 480 parameters, the experiment is replicated several times. Similar results are obtained as the best
 481 result reported in Table 6 and Fig. 5 (a)-(e). These experiments demonstrate that the LSNN
 482 method can capture the compound wave for non-convex flux problems as well.

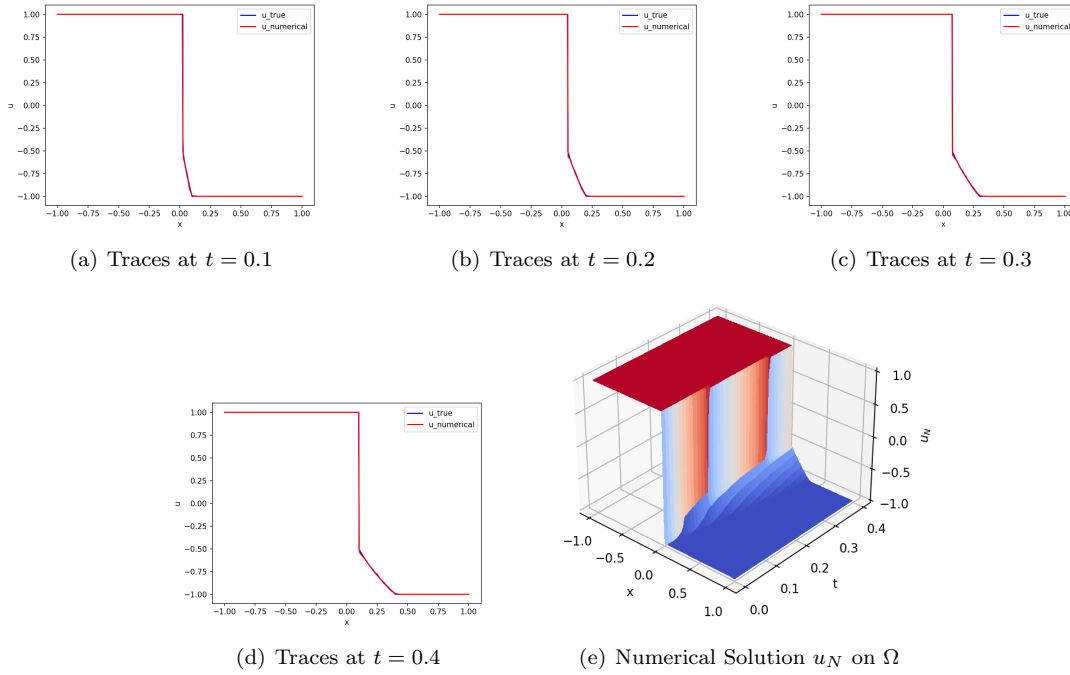


FIG. 5. Numerical results of Riemann problem with a non-convex flux $f(u) = \frac{1}{3}u^3$

483 **5.4. Two-dimensional problem.** Consider a two-dimensional inviscid Burgers equation,
 484 where the spatial flux vector field is $\tilde{\mathbf{f}}(u) = \frac{1}{2}(u^2, u^2)$. Given a piece-wise constant initial data

485 (5.2)
$$u_0(x, y) = \begin{cases} -0.2, & \text{if } x < 0.5 \text{ and } y > 0.5, \\ -1.0, & \text{if } x > 0.5 \text{ and } y > 0.5, \\ 0.5, & \text{if } x < 0.5 \text{ and } y < 0.5, \\ 0.8, & \text{if } x > 0.5 \text{ and } y < 0.5, \end{cases}$$

486 this problem has an exact solution given in [17].

487 The test problem is set on computational domain $\Omega = (0, 1)^2 \times (0, 0.5)$ with inflow boundary
 488 conditions prescribed by using the exact solution. Our numerical result using a 4-layer LSNN
 489 (3-48-48-48-1) with 3D $\mathbf{div}_\tau(\hat{\mathbf{m}} = \hat{\mathbf{n}} = \hat{\mathbf{k}} = 2)$ are reported in Table 7. The corresponding hyper
 490 parameters setting is as follows: $n_b = 5$, $\alpha = 20$, the first time block is trained with 30000 iteration
 491 where the first 10000 iterations are using learning rate 0.003 and the rest iterations are trained
 492 using learning rate of 0.001; all remaining time blocks are trained with 20000 iterations using fixed
 493 learning rate of 0.001. Fig. 6 presents the graphical results at time $t = 0.1, 0.3$, and 0.5 . This
 494 experiment shows that the proposed LSNN method can be extended to two dimensional problems
 495 and can capture the shock and rarefaction waves in two dimensions.

496 **6. Discussion and Conclusion.** The ReLU neural network provides a new class of approx-
 497 imating functions that is ideal for approximating discontinuous functions with unknown interface
 498 location [7]. Making use of this unique feature of neural networks, this paper studied the least-
 499 squares ReLU neural network (LSNN) method for solving scalar nonlinear hyperbolic conservation
 500 laws.

501 In the design of the LSNN method for HCLs, the numerical approximation of differential
 502 operators is a critical factor, and standard numerical or automatic differentiation along coordinate

TABLE 7
Relative L^2 errors of Riemann problem (shock) for 2D Burgers' equation

Network structure	Block	$\frac{\ u^k - u^k_\tau\ _0}{\ u^k\ _0}$
3-48-48-48-1	$\Omega_{0,1}$	0.093679
	$\Omega_{1,2}$	0.121375
	$\Omega_{2,3}$	0.163755
	$\Omega_{3,4}$	0.190460
	$\Omega_{4,5}$	0.213013

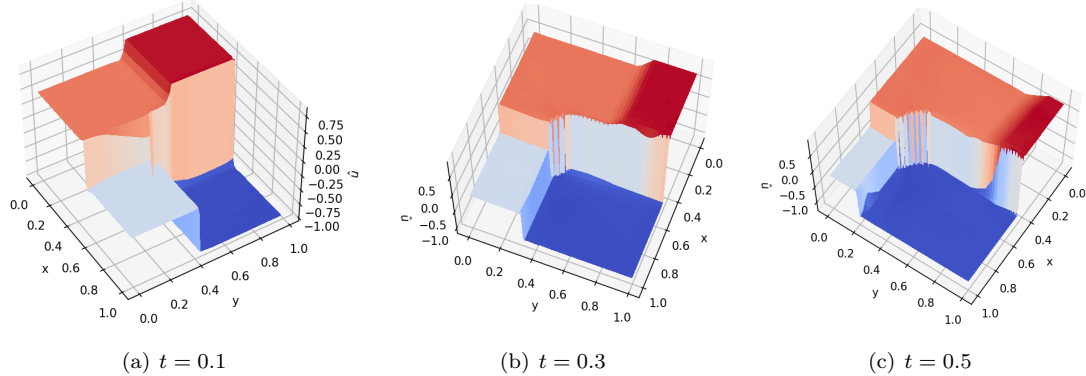


FIG. 6. Numerical results of 2D Burgers' equation.

503 directions can often lead to a failed NN-based method. To overcome this challenge, this paper
504 introduced a new discrete divergence operator \mathbf{div}_τ based on its physical meaning.

505 Numerical results for several test problems show that the LSNN method using the \mathbf{div}_τ does
506 overcome limitations of the LSNN method with conservative flux in [6]. Moreover, for the one
507 dimensional test problems with fluxes $f(u) = \frac{1}{4}u^4$ and $\frac{1}{3}u^3$, the accuracy of the method may be
508 improved greatly by using enough number of sub-intervals in the composite trapezoidal/mid-point
509 quadrature.

510 Compared to other NN-based methods like the PINN and its variants, the LSNN method
511 introduced in this paper free of any penalization such as the entropy, total variation, and/or
512 artificial viscosity, etc. Usually, choosing proper penalization constants can be challenging in
513 practice and it affects the accuracy, efficiency, and stability of the method.

514 Even though the number of degrees of freedom for the LSNN method is several order of magni-
515 tude less than those of traditional mesh-based numerical methods, training NN is computationally
516 intensive and complicated. For a network with more than one hidden layer, random initialization
517 of the parameters in layers beyond the first hidden layer would cause some uncertainty in training
518 NN (iteratively solving the resulting non-convex optimization) as observed in Section 5.2. This
519 issue plus designation of a proper architecture of NN would be addressed in a forthcoming paper
520 using the adaptive network enhancement (ANE) method developed in [27, 26, 8].

521

REFERENCES

- 522 [1] Y. Bar-Sinai, S. Hoyer, J. Hickey, and M. P. Brenner. Learning data-driven discretizations for partial differential
523 equations. *Proceedings of the National Academy of Science of USA*, 116 (31):15344–15349, 2019.
524 [2] P. Bochev and J. Choi. Improved least-squares error estimates for scalar hyperbolic problems. *Comput.
525 Methods Appl. Math.*, 1(2):115–124, 2001.

- 526 [3] F. Brezzi, L. D. Marini, and E. Süli. Discontinuous Galerkin methods for first-order hyperbolic problems.
527 *Math. Models Methods Appl. Sci.*, 14(12):1893–1903, 2004.
- 528 [4] E. Burman. A posteriori error estimation for interior penalty finite element approximations of the advection-
529 reaction equation. *SIAM J. Numer. Anal.*, 47(5):3584–3607, 2009.
- 530 [5] Z. Cai, J. Chen, and M. Liu. Finite volume least-squares neural network (fv-lsnn) method for scalar nonlinear
531 hyperbolic conservation laws, arxiv:2110.10895 [math.na]. 2021.
- 532 [6] Z. Cai, J. Chen, and M. Liu. Least-squares ReLU neural network (LSNN) method for scalar nonlinear
533 hyperbolic conservation law. *Appl. Numer. Math.*, 174:163–176, 2022.
- 534 [7] Z. Cai, J. Chen, and M. Liu. Least-squares ReLU neural network (LSNN) method for linear advection-reaction
535 equation. *J. Comput. Phys.*, 443 (2021) 110514.
- 536 [8] Z. Cai, J. Chen, and M. Liu. Self-adaptive deep neural network: Numerical approximation to functions and
537 PDEs. *J. Comput. Phys.*, 455 (2022) 111021.
- 538 [9] Z. Cai, J. Chen, M. Liu, and X. Liu. Deep least-squares methods: An unsupervised learning-based numerical
539 method for solving elliptic PDEs. *J. Comput. Phys.*, 420 (2020) 109707.
- 540 [10] B. Cockburn and C.-W. Shu. TVB Runge-Kutta local projection discontinuous galerkin finite element method
541 for conservation laws. *Math. Comp.*, 52:411–435, 1989.
- 542 [11] W. Dahmen, C. Huang, C. Schwab, and G. Welper. Adaptive petrov–galerkin methods for first order transport
543 equations. *SIAM J. Numer. Anal.*, 50(5):2420–2445, 2012.
- 544 [12] H. De Sterck, T. A. Manteuffel, S. F. McCormick, and L. Olson. Least-squares finite element methods and
545 algebraic multigrid solvers for linear hyperbolic PDEs. *SIAM J. Sci. Comput.*, 26(1):31–54, 2004.
- 546 [13] H. De Sterck, T. A. Manteuffel, S. F. McCormick, and L. Olson. Numerical conservation properties of
547 $H(\text{div})$ -conforming least-squares finite element methods for the burgers equation. *SIAM J. Sci. Com-
548 put.*, 26(5):1573–1597, 2005.
- 549 [14] L. Demkowicz and J. Gopalakrishnan. A class of discontinuous petrov–galerkin methods. part I: The transport
550 equation. *Comput. Methods Appl. Mech. Eng.*, 199(23-24):1558–1572, 2010.
- 551 [15] O. Fuks and H. Tehelepi. Limitations of physics informed machine learning for nonlinear two-phase transport
552 porous media. *J. Machine Learning for Modeling and Computing*, 1(1):19–37, 2020.
- 553 [16] D. Gottlieb and C.-W. Shu. On the Gibbs phenomenon and its resolution. *SIAM Review*, 39(4):644–668, 1997.
- 554 [17] J.-L. Guermond and M. Nazarov. A maximum-principle preserving C^0 finite element method for scalar
555 conservation equations. *Comput. Methods Appl. Mech. Eng.*, 272:198–213, 2014.
- 556 [18] A. Harten, B. Engquist, S. Osher, and S. R. Chakravarty. Uniformly high order accurate essentially non-
557 oscillatory schemes, III. In *Upwind and high-resolution schemes*, pages 218–290. Springer, 1987.
- 558 [19] J. S. Hesthaven. *Numerical Methods for Conservation Laws: From Analysis to Algorithms*. SIAM, 2017.
- 559 [20] J. S. Hesthaven and T. Warburton. *Nodal Discontinuous Galerkin Methods: Algorithms, Analysis, and
560 Applications*. Springer Science & Business Media, 2007.
- 561 [21] P. Houston, J. A. Mackenzie, E. Süli, and G. Warnecke. A posteriori error analysis for numerical approximations
562 of Friedrichs systems. *Numer. Math.*, 82(3):433–470, 1999.
- 563 [22] P. Houston, R. Rannacher, and E. Süli. A posteriori error analysis for stabilised finite element approximations
564 of transport problems. *Comput. Methods Appl. Mech. Eng.*, 190(11-12):1483–1508, 2000.
- 565 [23] D. I. Ketcheson, R. J. LeVeque, and M. J. del Razo. *Riemann Problems and Jupyter Solutions*. SIAM,
566 Philadelphia, 2020.
- 567 [24] D. P. Kingma and J. Ba. ADAM: A method for stochastic optimization. In *International Conference on
568 Representation Learning, San Diego*, 2015; arXiv preprint arXiv:1412.6980.
- 569 [25] R. J. LeVeque. *Numerical Methods for Conservation Laws*. Birkhäuser, Boston, 1992.
- 570 [26] M. Liu and Z. Cai. Adaptive two-layer ReLU neural network: II. Ritz approximation to elliptic PDEs. *Comput.
571 Math. Appl.*, 113:103–116, 2022.
- 572 [27] M. Liu, Z. Cai, and J. Chen. Adaptive two-layer ReLU neural network: I. best least-squares approximation.
573 *Comput. Math. Appl.*, 113:34–44, 2022.
- 574 [28] S. Osher. Riemann solvers, the entropy condition, and difference approximations. *SIAM J. Numer. Anal.*,
575 21:217–235, 1984.
- 576 [29] R. G. Patel, I. Manickam, N. A. Trask, M. A. Wood, M. Lee, I. Tomas, and E. C. Cyr. Thermodynamically
577 consistent physics-informed neural networks for hyperbolic systems. *J. Comput. Phys.*, 449, 2022.
- 578 [30] M. Raissi, P. Perdikaris, and G. E. Karniadakis. Physics-informed neural networks: A deep learning framework
579 for solving forward and inverse problems involving nonlinear partial differential equations. *J. Comput.
580 Phys.*, 378:686–707, 2019.
- 581 [31] P. L. Roe. Approximate Riemann solvers, parameter vectors, and difference schemes. *J. Comput. Phys.*,
582 43(2):357–372, 1981.
- 583 [32] C.-W. Shu. Essentially non-oscillatory and weighted essentially non-oscillatory schemes for hyperbolic conser-
584 vation laws. In *Advanced Numerical Approximation of Nonlinear Hyperbolic Equations*, pages 325–432.
585 Springer, 1998.
- 586 [33] C.-W. Shu and S. Osher. Efficient implementation of essentially non-oscillatory shock-capturing schemes. *J.
587 Comput. Phys.*, 77(2):439–471, 1988.
- 588 [34] J. Sirignano and K. Spiliopoulos. DGM: A deep learning algorithm for solving partial differential equations.
589 *J. Comput. Phys.*, 375:1139–1364, 2018.
- 590 [35] J. W. Thomas. *Numerical Partial Differential Equations: Finite Difference Methods*, volume 22. Springer
591 Science & Business Media, 2013.
- 592 [36] Z. Zhao, Y. Chen, and J. Qiu. A hybrid Hermite WENO scheme for hyperbolic conservation laws. *J. Comput.*

593 *Phys.*, 405:109175, 2020.

594 **7. Appendix.** In the appendix, we provide the proofs of Lemmas 4.2 and 4.3. First, denote
595 the integral and the mid-point/trapezoidal rule of a function φ over an interval $[0, \rho]$ by

$$596 \quad I(\varphi) = \int_0^\rho \varphi(s) ds \quad \text{and} \quad Q(\varphi; 0, \rho, 1) = \begin{cases} \rho \varphi(\rho/2), & \text{midpoint,} \\ \frac{\rho}{2}(\varphi(0) + \varphi(\rho)), & \text{trapezoidal,} \end{cases}$$

597 respectively. Let $p, q \in (1, \infty]$ such that $1/p + 1/q = 1$. It is easy to show the following error
598 bounds:

$$599 \quad (7.1) \quad |I(\varphi) - Q(\varphi; 0, \rho, 1)| \leq \begin{cases} C \rho^{2+1/q} \|\varphi''\|_{L^p(0, \rho)}, & \text{if } \varphi \in C^2(0, \rho), \\ C \rho^{1+1/q} \|\varphi'\|_{L^p(0, \rho)}, & \text{if } \varphi \in C^1(0, \rho). \end{cases}$$

600 *Proof of Lemma 4.2.* We prove Lemma 4.2 only for the mid-point rule because it may be
601 proved in a similar fashion for the trapezoidal rule. To this end, denote uniform partitions of the
602 intervals $[x_i, x_{i+1}]$ and $[t_j, t_{j+1}]$ by

$$603 \quad x_i = x_i^0 < x_i^1 < \dots < x_i^{\hat{m}} = x_{i+1}, \text{ and } t_j = t_j^0 < t_j^1 < \dots < t_j^{\hat{n}} = t_{j+1},$$

604 respectively, where $x_i^k = x_i + k\hat{h}$ and $t_j^k = t_j + k\hat{\delta}$; and $\hat{h} = h/\hat{m}$ and $\hat{\delta} = \delta/\hat{n}$ are the numerical
605 integration mesh sizes. By (7.1), we have

$$606 \quad \left| \int_{t_j^k}^{t_j^{k+1}} \sigma(x_i, x_{i+1}; t) dt - \hat{\delta} \sigma(x_i, x_{i+1}; t_j^{k+1/2}) \right| \leq C \hat{\delta}^{2+1/q} \|\sigma_{tt}(x_i, x_{i+1}; \cdot)\|_{L^p(t_j^k, t_j^{k+1})},$$

$$607 \quad \text{and} \quad \left| \int_{x_i^k}^{x_i^{k+1}} u(x; t_j, t_{j+1}) dx - \hat{h} u(x_i^{k+1/2}; t_j, t_{j+1}) \right| \leq C \hat{h}^{2+1/q} \|u_{xx}(\cdot; t_j, t_{j+1})\|_{L^p(x_i^k, x_i^{k+1})},$$

608 which, together with (4.3), (4.4), and the triangle and the Hölder inequalities, implies

$$609 \quad |K_{ij}|^{1/q} \|\mathbf{div}_\tau \mathbf{f}(u) - \text{avg}_\tau \mathbf{div} \mathbf{f}(u)\|_{L^p(K_{ij})} = |K_{ij}| \left| \text{avg}_{K_{ij}} \mathbf{div} \mathbf{f}(u) - \mathbf{div}_\tau \mathbf{f}(u(\mathbf{m}_{ij})) \right|$$

$$610 \quad \leq C \left\{ h \hat{\delta}^{2+1/q} \sum_{k=0}^{\hat{n}-1} \|\sigma_{tt}(x_i, x_{i+1}; \cdot)\|_{L^p(t_j^k, t_j^{k+1})} + \delta \hat{h}^{2+1/q} \sum_{k=0}^{\hat{m}-1} \|u_{xx}(\cdot; t_j, t_{j+1})\|_{L^p(x_i^k, x_i^{k+1})} \right\}$$

$$611 \quad \leq C \left\{ h \hat{\delta}^{2+1/q} \hat{n}^{1/q} \|\sigma_{tt}(x_i, x_{i+1}; \cdot)\|_{L^p(t_j, t_{j+1})} + \delta \hat{h}^{2+1/q} \hat{m}^{1/q} \|u_{xx}(\cdot; t_j, t_{j+1})\|_{L^p(x_i, x_{i+1})} \right\}.$$

612 This completes the proof of Lemma 4.2. \square

613 To prove Lemma 4.3, we need to estimate an error bound of numerical integration for piece-wise
614 smooth and discontinuous integrant over interval $[0, \rho]$.

615 **LEMMA 7.1.** *For any $0 < \hat{\rho} < \rho/2$, assume that $\varphi \in C^1((0, \hat{\rho})) \cap C^1((\hat{\rho}, \rho))$ is a piece-wise C^1*
 616 *function. Denote by $j_\varphi = |\varphi(\hat{\rho}^+) - \varphi(\hat{\rho}^-)|$ the jump of $\varphi(s)$ at $s = \hat{\rho}$. Then there exists a positive*
 617 *constant C such that*

$$618 \quad |I(\varphi) - Q(\varphi; 0, \rho, 1)| \leq C\rho^{1+1/q} \|\varphi'\|_{L^p((0, \rho) \setminus \{\hat{\rho}\})} + \begin{cases} \hat{\rho} j_\varphi, & \text{mid-point,} \\ \left| \frac{\rho}{2} - \hat{\rho} \right| j_\varphi, & \text{trapezoidal} \end{cases}$$

$$619 \quad (7.2) \quad \leq C\rho^{1+1/q} \|\varphi'\|_{L^p((0, \rho) \setminus \{\hat{\rho}\})} + \frac{\rho}{2} j_\varphi.$$

620 *Proof.* Denote the linear interpolant of φ on the interval $[0, \rho]$ by $\varphi_1(s) = \varphi(0) \frac{\rho - s}{\rho} + \varphi(\rho) \frac{s}{\rho}$.
 621 For any $s \in (0, \hat{\rho})$, by the fact that $\varphi(0) - \varphi_1(0) = 0$, a standard argument on the error bound of
 622 interpolant yields that there exists a $\xi_- \in (0, \hat{\rho})$ such that

$$623 \quad \varphi(s) - \varphi_1(s) = \varphi'(\xi_-)s - \frac{s}{\rho}(\varphi(\rho) - \varphi(0)),$$

624 which implies

$$625 \quad \int_0^{\hat{\rho}} (\varphi(s) - \varphi_1(s)) ds = \int_0^{\hat{\rho}} \varphi'(\xi_-)s ds - \frac{\hat{\rho}^2}{2\rho} (\varphi(\rho) - \varphi(0)).$$

626 In a similar fashion, there exists a $\xi_+ \in (\hat{\rho}, \rho)$ such that

$$627 \quad \int_{\hat{\rho}}^{\rho} (\varphi(s) - \varphi_1(s)) ds = \int_{\hat{\rho}}^{\rho} \varphi'(\xi_+)(s - \rho) ds + \frac{(\rho - \hat{\rho})^2}{2\rho} (\varphi(\rho) - \varphi(0)).$$

628 Combining the above inequalities and using the triangle and the Hölder inequalities give

$$629 \quad |I(\varphi) - Q_t(\varphi)| = \left| \int_0^{\hat{\rho}} \varphi'(\xi_-)s ds + \int_{\hat{\rho}}^{\rho} \varphi'(\xi_+)(s - \rho) ds + \frac{\rho - 2\hat{\rho}}{2} (\varphi(\rho) - \varphi(0)) \right|$$

$$630 \quad \leq \frac{1}{(1+q)^{1/q}} \rho^{1+1/q} (\|\varphi'\|_{L^p(0, \hat{\rho})} + \|\varphi'\|_{L^p(\hat{\rho}, \rho)}) + \left| \frac{\rho}{2} - \hat{\rho} \right| |\varphi(\rho) - \varphi(0)|$$

$$631 \quad \leq \frac{2^{1/q}}{(1+q)^{1/q}} \rho^{1+1/q} \|\varphi'\|_{L^p((0, \rho) \setminus \{\hat{\rho}\})} + \left| \frac{\rho}{2} - \hat{\rho} \right| |\varphi(\rho) - \varphi(0)|.$$

632 It follows from the triangle and the Hölder inequalities that

$$633 \quad |\varphi(\rho) - \varphi(0)| \leq \left| \int_{\hat{\rho}}^{\rho} \varphi'(s) ds \right| + \left| \int_0^{\hat{\rho}} \varphi'(s) ds \right| + j_\varphi$$

$$634 \quad \leq \rho^{1/q} (\|\varphi'\|_{L^p(0, \hat{\rho})} + \|\varphi'\|_{L^p(\hat{\rho}, \rho)}) + j_\varphi \leq (2\rho)^{1/q} \|\varphi'\|_{L^p((0, \rho) \setminus \{\hat{\rho}\})} + j_\varphi.$$

635 Now, the above two inequalities and the fact that $\left| \frac{\rho}{2} - \hat{\rho} \right| \leq \frac{\rho}{2}$ imply (7.2) for the trapezoidal rule.

636 To prove the validity of (7.2) for the mid-point rule, note that for any $s \in (0, \hat{\rho})$ we have

$$637 \quad \varphi(s) - \varphi(\rho/2) = \int_{\hat{\rho}}^s \varphi'(s) ds + \int_{\rho/2}^{\hat{\rho}} \varphi'(s) ds + \varphi(\hat{\rho}^-) - \varphi(\hat{\rho}^+)$$

$$638 \quad \leq (\hat{\rho} - s)^{1/q} \|\varphi'\|_{L^p(s, \hat{\rho})} + (\rho/2 - \hat{\rho})^{1/q} \|\varphi'\|_{L^p(\hat{\rho}, \rho/2)} + \varphi(\hat{\rho}^-) - \varphi(\hat{\rho}^+),$$

639 which, together with the triangle inequality, implies

$$640 \quad \left| \int_0^{\hat{\rho}} (\varphi(s) - \varphi(\rho/2)) ds \right| \leq \left(\frac{\rho}{2}\right)^{1+1/q} (\|\varphi'\|_{L^p(0,\hat{\rho})} + \|\varphi'\|_{L^p(\hat{\rho},\rho/2)}) + \hat{\rho}j\varphi.$$

641 Similarly, we have

$$642 \quad \left| \int_{\hat{\rho}}^{\rho} (\varphi(s) - \varphi(\rho/2)) ds \right| \leq \frac{2q}{1+q} \left(\frac{\rho}{2}\right)^{1+1/q} \|\varphi'\|_{L^p(\hat{\rho},\rho)}.$$

643 Now, (7.2) for the mid-point rule follows from the triangle inequality and the above two inequalities.
644 This completes the proof of the lemma. \square

645 Now, we are ready to prove the validity of Lemma 4.3.

646 *Proof of Lemma 4.3.* By the assumption, the discontinuous interface Γ_{ij} intercepts two hori-
647 zontal edges at (\hat{x}_i^l, t_l) for $l = j, j+1$. Without loss of generality, assume that $\hat{x}_i^j \in (x_i^{k_j}, x_i^{k_j+1})$
648 and $\hat{x}_i^{j+1} \in (x_i^{k_{j+1}}, x_i^{k_{j+1}+1})$ for some k_j and k_{j+1} in $\{0, 1, \dots, \hat{m}\}$. Let $\hat{I}_{ij} = (x_i^{k_j}, x_i^{k_j+1}) \cup$
649 $(x_i^{k_{j+1}}, x_i^{k_{j+1}+1})$. The same proof of Lemma 4.2 leads to

$$650 \quad \left\| \mathbf{div}_{\mathcal{T}} \mathbf{f}(u) - \text{avg}_{\mathcal{T}} \mathbf{div} \mathbf{f}(u) \right\|_{L^p(K_{ij})}$$

$$651 \quad \leq C \left\{ \frac{h^{1/p}\delta^2}{\hat{n}^2} \|\sigma_{tt}(x_i, x_{i+1}; \cdot)\|_{L^p(t_j, t_{j+1})} + \frac{h^2\delta^{1/p}}{\hat{m}^2} \|u_{xx}(\cdot; t_j, t_{j+1})\|_{L^p((x_i, x_{i+1}) \setminus \hat{I}_{ij})} \right\}$$

$$652 \quad + \frac{\delta}{(h\delta)^{1/q}} \sum_{l=j}^{j+1} \left| \int_{x_i^{k_l}}^{x_i^{k_l+1}} u(x; t_j, t_{j+1}) dx - \hat{h}u(x_i^{k_l+\frac{1}{2}}; t_j, t_{j+1}) \right|,$$

653 which, together with Lemma 7.1, implies

$$654 \quad \left\| \mathbf{div}_{\mathcal{T}} \mathbf{f}(u) - \text{avg}_{\mathcal{T}} \mathbf{div} \mathbf{f}(u) \right\|_{L^p(K_{ij})}$$

$$655 \quad \leq C \left(\frac{h^{1/p}\delta^2}{\hat{n}^2} + \frac{h^2\delta^{1/p}}{\hat{m}^2} \right) + \frac{\hat{h}\delta}{(h\delta)^{1/q}} \sum_{l=j}^{j+1} \left\{ C\hat{h}^{1/q} \|u_x(\cdot; t_j, t_{j+1})\|_{L^p((x_i, x_{i+1}) \setminus \{\hat{x}_i^l\})} + \llbracket u(\hat{x}_i^l, t_l) \rrbracket \right\}.$$

656 Now, (4.7) follows from $\hat{h} = h/\hat{m}$. This completes the proof of Lemma 4.3. \square